Optical imaging of treatment-naïve human NSCLC reveals changes associated with metastatic recurrence

Paola Monterroso Diaz[1], Jesse D. Ivers[1], Stephanie Byrum[2], Charles M. Quick[3], Konstantinos Arnaoutakis[4], Kyle P. Quinn[1], Narasimhan Rajaram[1]

[1]Department of Biomedical Engineering, University of Arkansas, Fayetteville, AR, 72701

[2]Department of Biochemistry and Molecular Biology, University of Arkansas for Medical Sciences, Little Rock, AR 72205, USA

[3]Department of Pathology, University of Arkansas for Medical Sciences, Little Rock, Arkansas 72205.

[4]Department of Internal Medicine, Division of Hematology/Oncology, University of Arkansas for Medical Sciences, Little Rock, Arkansas 72205.

The authors disclose no potential conflicts of interest.

Abstract

Lung cancer remains the leading cause of cancer deaths, comprising nearly 25% of all cancer deaths [1]. The five-year survival rate of patients with non-small cell lung carcinoma (NSCLC) remains significantly low given that over half present with locally advanced or metastatic disease at time of diagnosis, and experience tumor recurrence following therapeutic intervention [2,3]. Current evaluation techniques to assess treatment response are lacking, given they are implemented several weeks after treatment completion and are solely based on anatomical changes in tumor size, forgoing other criteria such as functional or metabolic changes. There is a critical need to identify surrogate markers early on following diagnosis, that aid in distinguishing patients based on their long-term outcome. Two photon microscopy (TPM) techniques provide non-invasive high-resolution information on cell metabolism within tissue by utilizing an optical redox ratio (ORR) of FAD/[NADH+FAD] autofluorescence. The goal of this study is to use the ORR and NADH fluorescence lifetime decay to identify measurable differences in optical endpoints of human NSCLC that are indicative of their long-term outcome. Twenty-nine treatment-naïve NSCLC specimens were classified into metastatic and non-metastatic groups according to subject-detail reports. The ORR and mean NADH lifetime were determined for each sample, revealing a significant increase in the ORR for the metastatic group. Given that KEAP1 expression has previously been associated with poor patient outcomes, we stained our samples for KEAP1 and found low KEAP1 expression regions to be associated with higher ORR. A deep learning network base on Inception-ResNet-v2 trained on imaging endpoints (AUC = 0.68) outperformed a model built with only clinicopathologic features (AUC = 0.45), when classifying tumors

based on their metastatic status. These results demonstrate the feasibility of using optical imaging of autofluorescence of metabolic cofactors to identify differences indicative of long-term patient outcome.

Introduction

Approximately 50% of non-small-cell lung cancer patients present with advanced stage at time of diagnosis, and are treated with some combination of radiation therapy, chemotherapy, immune therapy, and/or surgery [4–6]. Surgical resection remains the first line of treatment for early-stage patients diagnosed with non-small-cell lung cancer [7]. Historically, adjuvant chemotherapy has been the standard of care for Stage II-III NSCLC following surgical resection even though it only shows a 5% improvement in disease-free survival [8–10]. Despite these interventions, approximately 50% of patients experience recurrence within five years following surgery [11]. Identifying patients at high risk of recurrence following surgical resection is critical for optimizing treatment strategies and improving patient outcomes. Moreover, early detection of recurrence would enable timely intervention, and may guide the selection of patients for adjuvant therapies, thus minimizing overtreatment and unnecessary treatment related toxicities.

Despite advances in early diagnosis and treatment of NSCLC, a notable absence of established markers of recurrence in NSCLC remains. Currently the prognosis for NSCLC involves the tumor-node-metastasis (TNM) staging system, which incorporates tumor size, nodal involvement, and distal metastasis to stratify patients to four stages of disease [12,13]. While the TNM system provides valuable prognostic information, it presents certain limitations. Specifically, the survival time for patients within identical tumor stages varies widely, as does their incidence of recurrence [14–16]. Other studies have explored the potential of imaging-based markers of recurrence, leveraging morphological and pathological information obtained from radiological imaging modalities and histologic slides. Radiomics, a field that involves the extraction of many quantitative features from medical images (such as PET, CT, and MRI), has been utilized to provide additional information for treatment strategies and to develop models for NSCLC prognosis and treatment outcomes. For example, Wang et al. constructed a predictive model that incorporated both radiomic features and clinical variables to assess the risk of postoperative recurrence in NSCLC patients. Their results demonstrated that combining CT radiomics with clinical features achieved superior predictive performance compared to models based solely on radiomic of clinical variables. [17]. Predictive modeling has also been developed by harnessing morphological features extracted from hematoxylin and eosin (H&E) stained slides. Recent studies have explored the use of digital pathology and image analysis techniques to extract quantitative features from tumor histological slides. One notable study investigated the predictive value of models involving computerized extraction of nuclear and tumoral features from H&E slides, and found that the combination of nuclear shape, texture and architectural features successfully predicted recurrence in early-stage NSCLC patients [18]. While these studies and several others [19–21] have demonstrated the potential of imaging-based predictive models for NSCLC, there are important limitations to address. Traditional medical imaging modalities, such as

CT, provide valuable structural information but overall possess low spatiotemporal resolution and lack the ability to capture subcellular functional changes that occur within tumors. The heterogeneity of NSCLC at the subcellular level, including variations in cellular metabolism, may have significant implications for tumor behavior and risk of recurrence [22]. These functional and molecular changes typically precede morphological changes and necessitate imaging modalities capable of detecting such dynamics [23]. Two-photon microscopy emerges as a promising tool in this regard, offering non-invasive and high-resolution imaging capabilities to probe cellular function within tissue, and potentially provide markers of recurrence in NSCLC [24].Two-photon microscopy has an intrinsic depth sectioning ability and can penetrate deeper into tissue using near-infrared excitation wavelengths [25,26]. Two-photon excited fluorescence (TPEF) from nicotinamide and flavin adenine dinucleotides (NADH and FAD, respectively) can been quantified to determine [27–30][31–34][35,36][37]an optical redox ratio (ORR) of FAD/(NADH+FAD), which has been shown to be highly correlated with the ratio of intracellular cofactor concentrations NAD^+/(NADH+NAD^+) [27]. The ORR has been used in vitro and in vivo to track metabolic changes during cancer progression and characterize early stages of cancer development [28–31]. These imaging studies have demonstrated that proliferative cells are associated with a lower redox ratio indicative of an increased rate of glucose catabolism. The ORR has also been used to quantitatively assess response to therapy in organoids derived from various cancer types, including breast, colon, and pancreas, identifying heterogenous cellular subpopulations driving varied treatment-response [32–34]. Other studies [35,36], including work from our lab [37], have demonstrated that highly invasive and metastatic cancer cells resort to mitochondrial oxidative metabolism as indicated by an increase in the redox ratio. In addition to TPEF, fluorescence lifetime imaging microscopy (FLIM) is another technique that is sensitive to metabolic changes in the tumor microenvironment. FLIM measures the time a fluorophore remains in the excited state and is sensitive to changes in the molecular microenvironment, such as pH, temperature, viscosity, and protein-binding status [38,39]. FLIM has been used to investigate cellular metabolism by discriminating between the free and protein-bound states of NADH and establishing the relative amounts of these species to characterize biological samples [38,40]. For example, decreases in the protein-bound NADH lifetime were reported in pre-cancerous epithelial cells compared to normal epithelium, consistent with increased rates of glycolysis [41]. Similar findings were reported in a study involving human lung cancer samples, where the average fluorescence lifetime for NADH in the cancerous lung tissue was significantly shorter compared to normal tissue [42].

While *in vivo* optical measurements are preferred, and can be more easily performed on accessible tissues, practical constraints limit their feasibility, especially for measurements of more inaccessible tissues such as the lung. TPEF optical endpoints have previously been reported in *ex vivo* tissues, elucidating differences between normal and neoplastic lung [42,43], diabetic and non-diabetic wounds

[44], and HIV-1 infected tissue sections [45]. Jones et al. demonstrated that although the ORR from *ex vivo* skin wound frozen sections was significantly higher than that of *in vivo* measurements, the metabolic trend observed between groups was preserved [46]. Walsh et al reported similar findings when comparing optical endpoints between fresh and frozen-thawed hamster cheek pouch tissues, attributing the increase in ORR of frozen-thawed tissue to both a decrease in NADH fluorescence intensity and increase in FAD fluorescence intensity [47]. While not ideal, *ex vivo* frozen tissue sections provide unique access to otherwise inaccessible tumors, and optical imaging of these tissues still provide us with unique insight into underlying mechanisms of disease.

The overall goal of this study was to investigate the optical changes associated with long term outcome in treatment-naïve NSCLC tumors, and whether these optical endpoints can serve as markers of recurrence in NSCLC. To do this we utilized high-resolution optical microscopy and image processing techniques to generate quantitative markers of metabolic activity in cryosections of primary tumors. We found that NSCLC tumors with metastatic recurrence presented with increased ORR compared to those experiencing no future recurrence. Additionally, we trained a deep learning artificial neural network to predict metastatic status of patient derived primary tumors, based on whole-image data. We demonstrated improved performance of the trained convolution neural network presenting with a higher AUC when compared to logistic regression models involving clinicopathologic features alone.

Methods

Study Design

Twenty-nine NSCLC specimens were obtained from the Lung Cancer Biospecimen Resource Network (LCBRN) and the Cooperative Human Tissue Network (CHTN). These specimens consisted of a mixture of adenocarcinoma and squamous cell carcinoma at stage II of disease and were resected from the lung prior to the patient receiving any type of therapy (Figure 1A). For each tissue, a specimen and patient detail report was made available, listing follow-up information such as type of adjuvant therapy later received, metastatic status, and response to therapy. All patients in this cohort received adjuvant therapy, involving a combination of radiation and cisplatin and/or other chemotherapy drugs. The clinical detail reports were used to evaluate the follow-up data of each patient and classify them into groups that reflected their eventual outcomes (Figure 1B). Patients were classified into the metastatic group (N=12) if they presented with metastatic lesions throughout their follow-up and classified into the non-metastatic group (N=17) if they presented with no metastasis (Table 1). Similarly, patients were classified as responders (N=13) if presenting with no evidence of disease after their second year of follow-up. Conversely, if the patient presented with tumor recurrence, they were classified as non-responders (N=16). Seven of the non-responder tumors fell under the non-metastatic classification, while three of the responder tumors fell under the metastatic classification. All

specimens had been previously flash frozen in liquid nitrogen and upon receipt were sectioned in a Leica CM1860 cryostat (Wetzlar, Germany) into sections 30 µm thick and placed in -80ºC for storage until time of imaging (Figure 1C).

Table 1. Clinical characteristics of NSCLC patients

	Clinical Outcome (patient numbers)			
	Non-Responder	Responder	Metastatic	Non-metastatic
Diagnosis				
Adenocarcinoma	14	8	11	11
SCC	2	5	1	6
Stage				
II	16	13	12	17

Histopathology

Upon completion of two-photon imaging, NSCLC tissue sections were subjected to hematoxylin and eosin (H&E) staining and Verhoeff Van Gieson (VVG) elastin staining. H&E staining provided general morphological information, allowing the identification of various tissue components, namely tumor cells, necrotic and stromal regions. These regions were identified and characterized with the help of an expert pathologist at the University of Arkansas for Medical Sciences. VVG staining specifically highlighted elastin fibers as well as collagen within the tissue. A Hamamatsu NanoZoomer-SQ digital slide scanner was used to provide whole-slide histology images that were then used as reference images for the segmentation process of TPEF images (Supplementary Figure 1).

Acquisition of 755/855 nm two-photon excited fluorescence (TPEF)

Two-photon microscopy was used according to established methods previously described [89]. Imaging was performed using a two-photon microscope consisting of a Bruker Ultima Investigator Series laser scanning microscope (Middleton, Wisconsin), and an Ultrafast Ti:Sapphire laser (Insight X3, HP, Spectra Physics, Inc.). Samples were imaged (512x512 pixels; 13-bit depth; 0.876 pixels/µm; 1.6 µs pixel dwell time) with a 20x, 1.0 NA water-immersion objective (Olympus; Tokyo, Japan). The laser excitation source was tuned to 755 nm and 855 nm to collect NADH and FAD TPEF, respectively. Images were acquired using GaAsP photomultiplier tubes (PMTs) with a 460/20 nm bandpass filter for the 755 nm excitation, and a 525/50 nm filter for 855nm excitation. Three to five regions of interest were imaged per sample.

Fluorescence lifetime imaging (FLIM) at 755 nm

NADH FLIM images were acquired from the same regions of interest as TPEF. FLIM images were processed using SPCImage 8.5 (Becker & Hickl Gmbh; Berlin, Germany). Images were collected over an integration time of 2 min (pixel dwell time of 0.8 µs) and lifetime decay curves were fit to a bi-

exponential model to ascertain the free and long lifetime components.

Image processing and quantitative analysis

Autofluorescence intensity images were normalized to laser power and PMT gain calibrated to µM concentrations of fluorescein (Figure 2A) [27]. Manual-traced masks were generated by using histological (H&E and VVG stains) images as references to isolate tumor cells from elastin-rich and necrotic regions within TPEF images from NSCLC tissue sections. In addition to manually-traced masks, Otsu's method was applied in a custom MATLAB script to create inverse masks that specifically highlighted areas of elastin and necrotic regions within TPEF images (Figure 2B). These masks were combined to effectively isolate tumor cells of interest and the resulting mask was applied to the corresponding redox ratio and FLIM images. A pixel-wise optical redox ratio [FAD/(NADH+FAD)] was calculated with previously normalized TPEF images, and an average of the redox ratio for each field of view (as well as an average for all FLIM parameters) was calculated from ORRs located only within the masked regions (Figure 2C, E).

Proteomics of NSCLC samples

Proteomic analyses and bioinformatics of the human NSCLC samples was performed at the IDeA National Resource for Quantitative Proteomics (Little Rock, AR) to determine changes in metabolic pathways to correlate to and validate the optical metabolic endpoints. In brief, 150 µg of whole cell lysate protein from each tumor was trypsin digested using the FASP procedure. UPLC off-line peptide fractionation with basic pH reverse-phase chromatography (bRPLC) was used to fractionate peptides into 40 fractions. Each fraction was resolved by in-line acidic pH reverse-phase chromatography with a nanoACQUITY UPLC system coupled to a Thermo Orbitrap Eclipse mass spectrometer. High resolution MS and MS/MS data was collected. Proteins were identified with MaxQuant (<1% FDR). A label-free intensity-based quantitation approach termed iBAQ was used [48,49] to determine the differentiating levels of proteins between groups. Log2-transformed iBAQ data was analyzed using 2-sample t-tests to conduct pairwise comparisons among the groups. Pairwise differences in group means were calculated along with unadjusted P values. Unadjusted P values were converted to q-values using the FDR procedure [50]. A protein was declared to be differentially expressed if (a) any 2 of its 3-group means were different by ≥1 log2 units (a ≥2x change) and (b) the difference in question had an FDR q≤0.05. Pathway analyses were carried out using IPA. Metabolically relevant pathways were explored and proteins that are differentially expressed within these pathways were identified within each treatment group.

KEAP1 immunofluorescence staining

Adjacent tissue slides to those previously used for TPM imaging, were selected for

immunofluorescence staining. Briefly, slides were fixed with paraformaldehyde, blocked with 10% goat serum, and exposed to rabbit primary antibody against KEAP1 (dilution 1: 200, Proteintech, Chicago, IL), followed by anti-rabbit secondary antibody (Alexa Fluor 568, Invitrogen, Carlsbad, CA). Five different tumors were selected for staining based on tissue section integrity and availability of sections adjacent to those previously imaged with TPM.

Image processing and analysis for ORR maps and immunofluorescence stains

For immunofluorescence stains, thresholds at 0.33 and 0.66 were used in a custom MATLAB script to generate masks for low, medium, and high regions of KEAP1 expression. Optical redox ratio maps were stitched together to generate mosaic ORR maps for each tissue section. Mosaic maps from both ORR images and immunofluorescent stains were then registered according to previously described methods [51]. Following registration, masks from low, medium, and high KEAP1 expression levels were overlaid on the ORR maps to generate ORR distributions for each level of KEAP1 expression.

Statistical analysis

Nested one-way analysis of variance (ANOVA) was used to identify statistically significant differences in the optical redox ratio, mean NADH lifetime, and A1/A2 ratio between groups. Specific fields of view nested within each tissue section, nested within each patient, were designated as random effects. Post hoc analysis was conducted using Tukey's HSD tests, and statistical significance was defined as $p<0.05$. All statistical analysis was performed using JMP® Pro 17.

Logistic regression modeling

We conducted a retrospective analysis on the NSCLC patient cohort. The dataset comprised information from 28 patients, encompassing demographic characteristics as well as pre-op, post-op and follow-up data. One patient was excluded from the analysis based on lack of information on features considered for the analysis, bringing the total down to 28 patients. The clinical data was collected from subject-detail reports, including sex (male or female), age, BMI, smoking status (never, former, or current), smoking pack years, histology subtype (adenocarcinoma or squamous cell carcinoma, and metastatic status. These variables were selected based on their potential prognostic significance and relevance to NSCLC progression [52–56]. In addition to clinical data, we also included optical endpoints as variables: optical redox ratio (ORR), mean NADH lifetime, and bound fraction ratio [A2/(A1+A2)].

A logistic regression model was used to predict metastatic status based on the selected predictor variables. Logistic regression is suitable for binary classification and provides estimates of the probability of the occurrence of an event. Nineteen patients (training group) were randomly selected to build the model, and the remaining nine formed the validation group. Two separate models were

built, one using only the clinical data and the second using only optical data. To evaluate classification performance, receiver operating characteristic (ROC) curves were used for each model. Logistic regression models were generated using MATLAB R2023b along with the Statistics and Machine Learning Toolbox. The logistic regression equations for clinical and optical parameters respectively, were as follows:

$$logit(y) = -29.7 + 0.26[Age] + 0.73[Sex] + 0.37[BMI] + 0.02[Smoking\ Status] + 0.02[Pk\ Yrs] - 0.54[Histology]$$

$$logit(y) = 4.52 - 0.88[ORR] - 0.001[TauM] - 5.14[BoundFraction]$$

Inception-ResNet-v2 Based Deep Learning

Artificial Neural Network Modelling

Using the same optical parameters, we trained a deep artificial neural network using stacks of manually masked whole-images (in contrast to patient-wise means use in logistic regression) to predict metastatic. The image stack was composed of ORR, mean NADH lifetime, and bound fraction images. This approach allowed us to evaluate the classification efficacy when high-resolution spatial information is preserved at model inputs.

The dataset was split randomly on a patient-wise basis into training and evaluation sets with the condition that the test set included at least three patients of each class: nonmetastatic and metastatic. The remaining patients were used for training. Importantly, all images from a given patient were restricted to a single set to prevent data leakage.

To meet dataset size demands of deep learning training, image data were augmented by cropping each 512 x 512 image into a five 256 x 256 images by cropping each corner and the center. Although this augmentation method introduces overlap between samples, we mitigated overfitting by randomly flipping and rotating image stacks each time they were accessed. Vertical and horizontal flips occurred at a rate of p = 0.25 with random rotations ranging from -180 to 180 degrees. These transformations helped prevent the model from learning orientation-specific features.

All images were normalized prior to forward pass and at inference to improve model stability and convergence time. Each parameter was normalized by the dataset-wide mean and standard deviation for all masked images of that parameter using the following equation:

$$x_i = \frac{x_i - \bar{x} - 3s_x}{6s_x}$$

where x_i is the individual image, $\bar{x}$ is the masked dataset-wide mean of the optical parameter and s_x is the masked dataset-wide standard deviation of the optical parameter. This normalization method

scales values within 3 standard deviations from the mean to between 0 and 1, effectively mapping the central portion of the data to the interval [0, 1]. Note that the subtraction and division operations in the equation are element-wise operations applied to each pixel of the image.

A pretrained convolutional neural network backbone was used to extract features from each image, which were then input into a binary classifier based on a simple multilayer perceptron (MLP) head regularized with random dropouts. We used the Inception-ResNet-v2 model [57] pretrained on ImageNet as the backbone. Feature map outputs were averaged and input into the MLP head composed of two hidden layers with 256 and 64 neurons each, and a single output neuron. To regularize training, dropouts of p = 0.10 were used at the feature map inputs (i.e. between the backbone and the head) and between the hidden layers of the MLP head. A dropout of p = 0.20 was used between the input layer and the first hidden layer of the MLP head (Fig. 3). This architecture was inspired by [58] with modifications to output a single binary class probability.

Hyperparemeters were optimized through multiple iterations with various learning rates and training times, while binary cross entropy loss was optimized and tracked to determine the efficacy of training. Ultimately, the final model was trained for 350 epochs at a learning rate of 1e-5 using an Adam optimizer and batch size of 64. Given the small dataset size, training was limited to the head for the first 150 epochs, while the backbone was frozen at the pretrained parameters. After 150 epochs, the final inception-resnet module (Inception-ResNet-C in Fig. 3) and final convolution (1 x 1 2D Conv in Fig. 3) of the backbone was unfrozen and allowed to train for 100 epochs. For the final 100 epochs, the entire model was unfrozen and trained.

Generalized model performance was assessed through cross validation, which was limited to 3 folds due to the limited number of patients, ensuring each test set comprised unique sets of both metastatic and non-metastatic patients, with a minimum of 3 patients from each class within the set. Due to missing data of some image modalities from 5 patients, the total number of patients considered was 23, with 11 metastatic and 12 non-metastatic cases. For cross-validation, class counts in the test set are outlined in Table 2. Mean ROC-AUC for all models in cross-validation was used as the final evaluation criterion.

Table 2. Dataset distributions for 3-Fold Cross Validation

Train and Test Set Distributions						
	Patient Classes in Test Set		Image Count		Fraction of total	
Fold	Metastatic	Non-Metastatic	Train	Test	Train	Test
1	4	4	435	230	0.65	0.35
2	4	4	440	225	0.66	0.34
3	3	4	455	210	0.68	0.32

The entire deep learning portion of this study was programmed in Python using Pytorch (code available on GitHub at https://github.com/jiversivers/nsclc.git). The model was trained and tested using a single NVIDIA A100 GPU. This portion of the research is supported by the Arkansas High Performance

Computing Center which is funded through multiple National Science Foundation grants and the Arkansas Economic Development Commission.

Results

Optical redox ratio is significantly higher in treatment-naïve NSCLC that had metastatic recurrence

Figures 4A and 4B present representative NADH and FAD intensity images from the non-metastatic and metastatic groups. Both tumors shown here are adenocarcinomas. Elastin structures and necrotic areas were avoided as best as possible during imaging, and during image processing, any additional elastin/necrotic areas present in the images were masked out and not included in the calculation of the optical redox ratio (Fig. 4C, 4D). We observed a statistically significant increase in the average optical redox ratio ($p=0.0415$) of the metastatic group compared with the non-metastatic group (Fig. 4E). This finding is consistent with previous work from our lab revealing increases in the redox ratio with increasing metastatic potential in cells, as well as other studies from other labs highlighting a decrease in NADH concentration in metastatic cancer [35,57]. These results demonstrate that there are measurable differences in metabolic imaging-based endpoints of NSCLC tumors based on their eventual outcome that can be exploited to evaluate long-term outcome in treatment-naïve tumors.

To further characterize changes in the metabolic profiles of the NSCLC samples, we also analyzed the FLIM images (Fig. 5A, B). NADH presents very different lifetimes depending on whether it is free or protein-bound [40]. Bi-exponential decay fit models were used to separate the short (A1) and long (A2) lifetime components of free and bound NADH, respectively. A1 and A2 are the respective relative contributions to the total fluorescence. Figure 5C reveals no significant changes in the mean NADH lifetime when comparing non-metastatic and metastatic tumors. No significant changes were found in the rest of lifetime parameters either (Figure 5D-F).

KEAP1 found to be dysregulated in stage II NSCLC with poor long-term outcome

Following proteomic analyses, key proteins such as the kelch-like ECH-associated protein 1 (KEAP1) were identified as differentially expressed in the responder vs non-responder tumors (Supplementary Figure 2). The KEAP1-nuclear factor erythroid-2-related factor-2 (Nrf2) pathway plays a key role in protecting cells from oxidative stress and has been linked to resistance to chemotherapy, radiation, and targeted therapies in NSCLC [58]. Previous studies have shown how low or absent KEAP1 expression is linked to a poorer overall survival in NSCLC [59]. Considering the dysregulation in KEAP1 expression in our cohort of NSCLC tumors, and the role KEAP1 plays in metabolic rewiring, we decided to investigate the association of KEAP1 expression with the ORR.

To evaluate the relationship between the KEAP1 expression and optical endpoints, tumor sections from serial slides adjacent to TPM sections were stained for KEAP1 (Figure 6B). Images from these

immunofluorescent stains were then registered to ORR mosaic maps (Figure 6C). Areas of low, medium, and high KEAP1 distribution were isolated, and ORR distributions from these areas were analyzed via one-way ANOVA comparison. We found regions of low KEAP1 expression to present with significantly higher ($p = 0.035$) (Figure 6D).

When considering clinical features alone, the logistic regression model did not identify any statistically significant predictors of metastatic status among the selected clinical variables, including sex, age, histology subtype, smoking status, and smoking pack years. Despite including these clinically relevant factors, Figure 7 shows an AUC of 0.45, indicating that clinical features alone were insufficient to predict metastatic status among this cohort of NSCLC patients. Conversely, when evaluating optical features independent from clinical such as the ORR, mean NADH lifetime, and bound ratio fraction, the logistic regression model revealed even poorer classification performance, presenting a lower AUC of 0.125. In view of the highly heterogenous sample data across metastatic and non-metastatic groups, this did not come as a surprise when we consider single optical parameter data points per patient, forsaking the wealth of information within the ORR and lifetime maps available for each patient. In light of this, we were interested in pursuing a more robust deep learning approach that incorporated entire imaging datasets that would allow to identify a larger number of features within each tumor that are otherwise overlooked in models that consider only one datapoint per subject. To this end, we trained an Inception-ResNet-v2 based classifier on manually masked image stacks of ORR, mean NADH lifetime, and bound fraction images. Over 3 folds, this model outperformed both aforementioned models with an average ROC-AUC of 0.68 ± 0.0638 across 3 folds (Figure 8).

Discussion

Two-photon imaging of cellular metabolism has been used in various contexts, such as metabolic changes during cancer progression, differentiation between normal and cancerous tissue, and monitoring stem cell differentiation [27,30,31]. In addition, researchers have also used optical metabolic imaging of tumor organoids to investigate treatment response of cancers of the pancreas, head and neck, and breast [60–62]. Specifically, previous studies have linked increases in the ORR with poor prognosis. Using a human melanoma mouse xenograft model with high and low metastatic risk, Peng et al. found that the more invasive and metastatic tumors were more oxidized compared to the indolent and less metastatic ones, presenting with an increase in ORR and lower NADH [63]. Within the context of human NSCLC, optical imaging has mainly been utilized for characterization and quantification of the structural makeup of NSCLC, and for diagnostic purposes, in differentiating lung tumor from surrounding healthy tissue [42,43,64,65]. Wang et al. utilized a combination of TPEF and second-harmonic generation (SHG) signals to differentiate cancerous from non-cancerous frozen-

thawed lung tissues [64]. Jain et al. also used TPM to characterize histopathological features in fresh NSCLC and conducted a blinded diagnostic analysis using TPM images, presenting both TPEF and SHG signals, that successfully differentiated neoplastic from nonneoplastic lung tissue [66]. Using a compact, portable microscope, Huizen et al. combined third and second harmonic generation (THG/SHG) and TPEF signals for the rapid identification and characterization of tissue architecture and cellular morphology in *ex vivo* fresh lung tissue. They found that the THG/SHG/TPEF images presented more information when compared to standard histopathology, positioning THG/SHG/TPEF as a promising tool for clinical intraoperative evaluation of NSCLC tissue [67]. In non-human lung tissues, Pavlova et al. utilized TPM to investigate a murine model of lung cancer and reported distinct morphological and spectral differences between *ex vivo* neoplastic lung and normal [43].

In comparison to previous studies utilizing TPM to investigate normal and NSCLC tissues, we report on a tumor-to-tumor comparison, aiming to determine whether optical markers from TPM can distinguish tumors based on their metastatic outcomes. We employed image masks that isolate tumor cells within all experimental groups and remove elastin and necrotic areas to eliminate the confounding effects of these components. This approach provides a more accurate and straightforward assessment of the optical characteristics of tumor cells within the NSCLC environment. Moreover, through the co-registration of immunohistochemistry and TPEF images, we were able to detect associations between proteomics and imaging markers. We utilized a custom Matlab code to perform manual registration of both the ORR map (fixed image) and its corresponding immunohistochemical stain (moving image) by selection of two points on each image. Manual selection of the two-point pairs were based on similar features clearly identified in both images. Due to the immunostaining being performed on a tissue section from an adjacent serial slide, certain challenges were encountered in registering both images. To address registration error, manual selection point pairs were performed three different times, and percent errors between reference points in fixed and moving images were calculated and found to be less than 5% in both x and y. By combining both molecular and optical information, these techniques enable a more comprehensive molecular characterization of NSCLC.

The higher ORR observed in the metastatic tumor group proves consistent with previous work from our lab revealing increases in the ORR with increasing metastatic potential in cells, as well as other studies reporting a decrease in NADH concentration in metastatic cancers [35,57]. While metastatic and non-metastatic tumors did not exhibit a statistically significant difference in FLIM parameters, they did display notable variations in their data distributions as depicted by the violin plots (Fig 4). These distributions point to inherent heterogeneity and complexity within these tumors. This variability may be due to a multitude of factors, including inter and intra-tumoral biological variability, and the highly heterogeneous metabolic landscape of NSCLC wherein both enhanced glycolysis and oxidative phosphorylation have been reported on within individual tumors[22].

In addition to optical imaging, proteomic analyses were conducted, revealing dysregulated expression of KEAP1 in NSCLC tumors with poor long-term outcome. In our hands, we observed that low KEAP1, which is associated with poor long-term outcome, overlapped exclusively with regions of high ORR, which we have found in metastatic cancer cells. Gong et al showed how activation of the KEAP1/NRF2 pathway decreases intracellular ROS levels [69]. Their results revealed significantly decreased ROS levels in KEAP1-mutated lung cancer cells, leading them to conclude that KEAP1 loss is linked to increased resistance of LC cells to oxidative stress. The KEAP1/NRF2 pathway has been shown to play a key role in regulating mitochondrial metabolism, and thus in cancer progression, by directly affecting the transcription of genes heavily involved in the respiratory chain complex [70]. Alterations in the KEAP1/NRF2 pathway has been associated with dysregulated metabolism in cancer, including rewiring of glucose metabolism and lipid metabolism [71–73]. In the context of mutated/depletion of KEAP1, previous studies report on NRF2 activation, leading to a highly reductive tumor microenvironment with an increased $NADH/NAD^+$ ratio and downregulated ROS levels [74]. Within our context of optical endpoints, this would translate into a lower ORR. However, in a subset of five adenocarcinoma samples, we observe that lower KEAP1 is associated with a higher ORR, and high KEAP1 expression was associated with lower ORR. In previous work, we have shown that increased ROS levels in lung cancer cells following treatment with a HIF-1 inhibitor were associated with an increase in ORR [75]. Further investigation into the role of ROS within these samples is required to discern these trends, given that the interplay between ROS and cellular redox state is complex and still not fully understood [76]

Diagnosis and treatment of NSCLC can prove challenging and accurate prediction of long-term outcomes is important for guiding treatment decisions and improving patient outcomes. Predictive modeling can be used to identify important risk factors and predictors of long-term outcome in NSCLC patients. Currently the prognosis for NSCLC involves the tumor-node-metastasis (TNM) staging system, which incorporates tumor size, nodal involvement, and distal metastasis to stratify patients to four stages of disease [12,13]. While the TNM system provides valuable prognostic information, it presents certain limitations. Specifically, the survival time for patients within identical tumor stages varies widely, as does their response to treatment [14–16]. Limitations are also seen when considering clinical features for predictive modeling of long-term outcome of NSCLC patients. The goal of this study was also to identify potential variables that aid in predicting the metastatic status of NSCLC patients by constructing a logistic regression model that combines optical marker and clinicopathologic features. Although we did not find improved classification performance in the model involving only optical features, we recognize this approach was limited due to its use of means calculated over entire tumor images for each patient. We were interested in using whole image data for deep learning classification techniques that more accurately categorize NSCLC tumors. Due to the limited dataset

size, our performance was limited, and we were careful to protect against overfitting. Despite this, the improved performance compared with other models in this study, we believe, shows the promise of deep learning models, particularly those that preserve the high-resolution spatial relationships of image data, show prognostic promise. Larger datasets will provide for more robust training that can both increase performance and improve generalizability. Furthermore, the feature-extractor backbone can be probed to investigate what features at the input are most predictive. This can be used to further refine models to limit the computational weight of a model. In this study, we elected not to perform this post-hoc feature selection, because performance was already at a lower limit. Together, these results demonstrate the feasibility of using optical imaging of autofluorescence and lifetimes of cellular metabolic cofactors to determine measurable differences in metabolic imaging-based endpoints of NSCLC tumors, based on their eventual outcome.

Figures

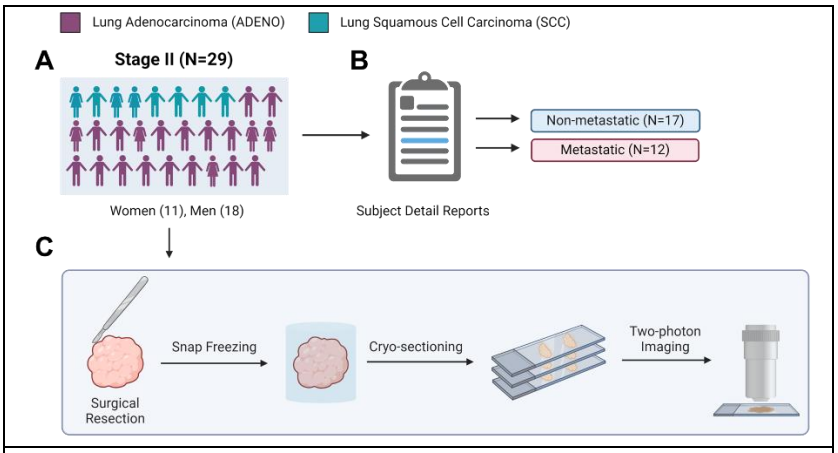

Figure 1. Overview of study design. Twenty-nine (29) NSCLC samples were collected prior to treatment, flash-frozen and stored. Upon receipt of samples, they were sectioned and mounted on slides for optical imaging.

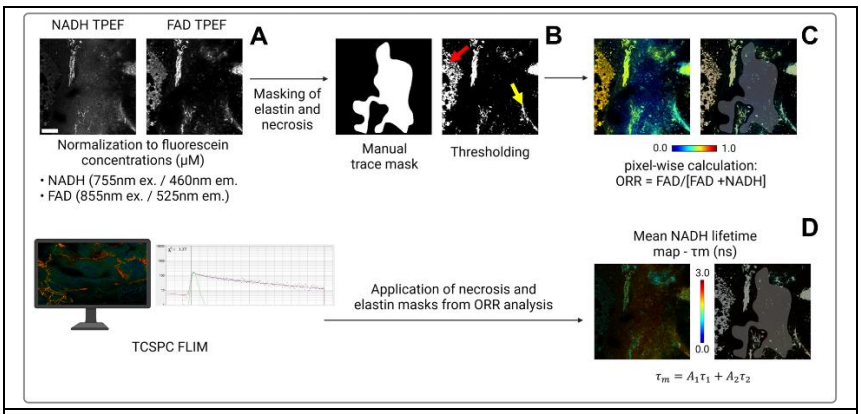

Figure 2. Image processing workflow for TPEF imaging and FLIM. Raw two-photon excited fluorescence intensity images (A) were processed with manual trace masks to exclude elastin (yellow arrow) and necrosis (red arrow) contributions (B). Pixel-wise calculations of the optical redox ratio were generated (C). Masks previously generated for ORR maps were also applied to NADH FLIM images (E).

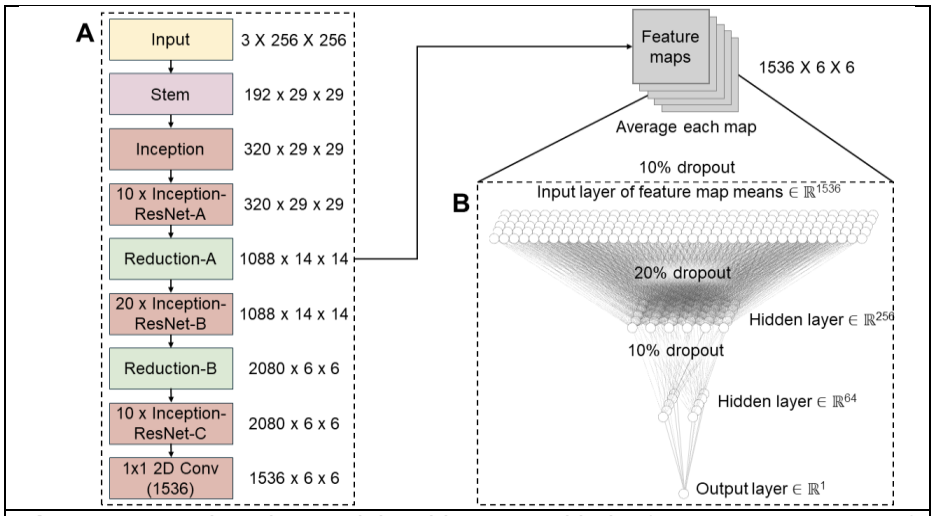

Figure 3. Deep learning model architecture, with the feature-map outputs of Inc**e**ption-ResNet-v2 backbone (A) shown averaged and input into the classifier head (B).

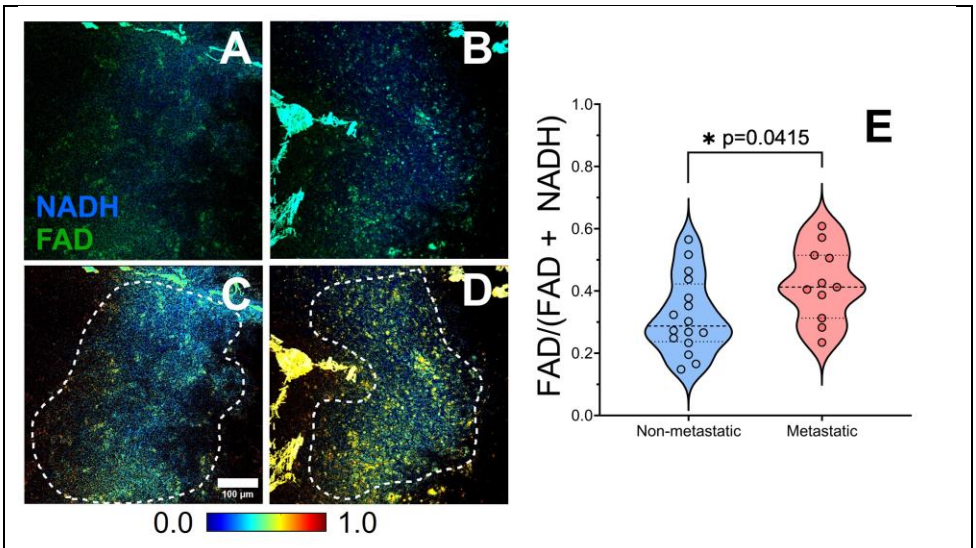

Figure 4. Normalized intensity images displaying NADH (blue) and FAD (green) signal (**A**, **B**) for representative ORR maps from non-metastatic (**C**) vs. metastatic tumors (**D**). A statistically significant increase in the optical redox ratio was observed in the metastatic tumor group when compared to non-metastatic (**E**)**.** Each data point represents a patient. Scale bar: 100 µm.

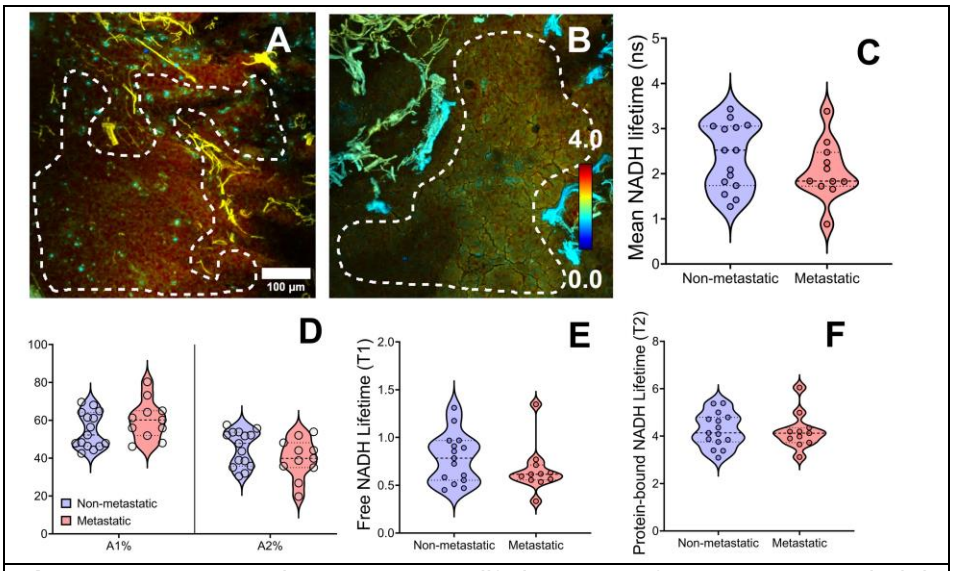

Figure 5. Representative mean NADH lifetime maps from non-metastatic (**A**) vs. metastatic tumors (**B**). Quantification of the average mean NADH lifetime and other lifetime parameters revealed no significant differences between metastatic and non-metastatic tumors (C-F). Each data point represents a patient. Scale bar: 100 µm.

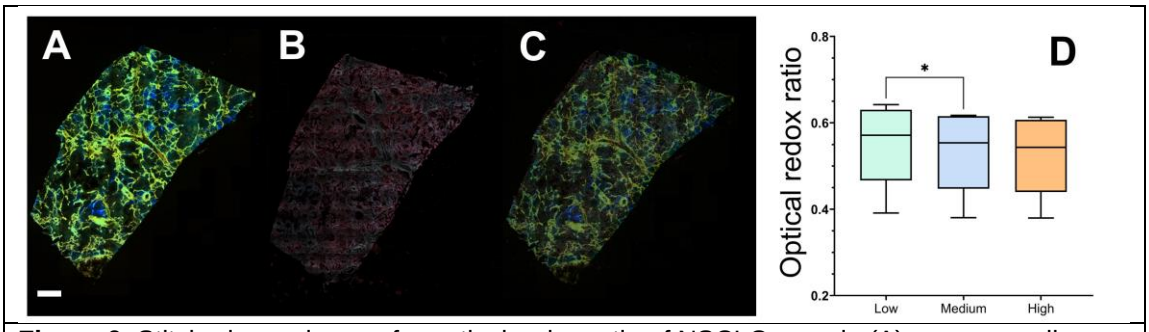

Figure 6. Stitched mosaic map for optical redox ratio of NSCLC sample (A), corresponding KEAP1 stain from serial slide (B) and resulting registration from both images (C). Quantification of the average mean ORR over each region of KEAP1 expression revealed a lower ORR for the medium KEAP1 expression regions compared to low (p<0.). Scale bar at 500 µm.

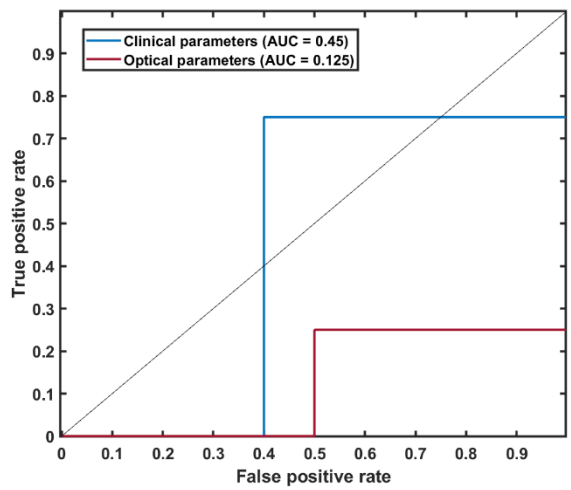

Figure 7. Comparison of receiver operating characteristic (ROC) curves for logistic regression model with clinicopathologic variables (red line) and optical features (blue line).

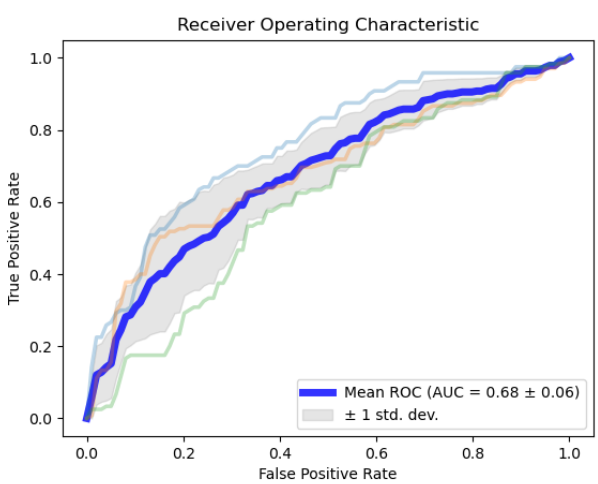

Figure 8. Receiver operating characteristic (ROC) curve for deep learning model with each fold of cross validation shown in thin lines (fold 1 in blue, 2 in orange, and 3 in green) and the mean shown in thick blue with ±1 standard deviation

References

1. H. Sung, J. Ferlay, R. L. Siegel, M. Laversanne, I. Soerjomataram, A. Jemal, and F. Bray, "Global Cancer Statistics 2020: GLOBOCAN Estimates of Incidence and Mortality Worldwide for 36 Cancers in 185 Countries," CA Cancer J Clin (2021).
2. H. Uramoto and F. Tanaka, "Recurrence after surgery in patients with NSCLC," Transl Lung Cancer Res **3**(4), 242 (2014).
3. T. TAMURA, K. KURISHIMA, K. NAKAZAWA, K. KAGOHASHI, H. ISHIKAWA, H. SATOH, and N. HIZAWA, "Specific organ metastases and survival in metastatic non-small-cell lung cancer," Mol Clin Oncol (2015).
4. J. R. Molina, P. Yang, S. D. Cassivi, S. E. Schild, and A. A. Adjei, "Non-small cell lung cancer: Epidemiology, risk factors, treatment, and survivorship," in *Mayo Clinic Proceedings* (2008).
5. E. Felip, N. Altorki, C. Zhou, T. Csőszi, I. Vynnychenko, O. Goloborodko, A. Luft, A. Akopov, A. Martinez-Marti, H. Kenmotsu, Y. M. Chen, A. Chella, S. Sugawara, D. Voong, F. Wu, J. Yi, Y. Deng, M. McCleland, E. Bennett, B. Gitlitz, and H. Wakelee, "Adjuvant atezolizumab after adjuvant chemotherapy in resected stage IB–IIIA non-small-cell lung cancer (IMpower010): a randomised, multicentre, open-label, phase 3 trial," The Lancet (2021).
6. G. T. Gibney, L. M. Weiner, and M. B. Atkins, "Predictive biomarkers for checkpoint inhibitor-based immunotherapy," Lancet Oncol (2016).
7. A. Lackey and J. Donington, "Surgical Management of Lung Cancer," Semin Intervent Radiol **30**(2), 133 (2013).
8. A. J. Wozniak and S. M. Gadgeel, "Adjuvant therapy for resected non-small cell lung cancer," Ther Adv Med Oncol **1**(2), 109 (2009).
9. R. Arriagada, B. Bergman, A. Dunant, T. Le Chevalier, J.-P. Pignon, J. Vansteenkiste, and International Adjuvant Lung Cancer Trial Collaborative Group, "Cisplatin-Based Adjuvant Chemotherapy in Patients with Completely Resected Non–Small-Cell Lung Cancer," New England Journal of Medicine (2004).
10. J. P. Pignon, H. Tribodet, G. V. Scagliotti, J. Y. Douillard, F. A. Shepherd, R. J. Stephens, and T. Le Chevalier, "Lung Adjuvant Cisplatin Evaluation (LACE): A pooled analysis of five randomized clinical trials including 4,584 patients," Journal of Clinical Oncology (2006).
11. T. Takenaka, T. Yano, K. Yamazaki, T. Okamoto, M. Hamatake, M. Shimokawa, and M. Mori, "Survival after recurrence following surgical resected non-small cell lung cancer: A multicenter, prospective cohort study," JTCVS Open **10**, 370–381 (2022).
12. D. Pouli, E. M. Genega, T. B. Sullivan, K. M. Rieger-Christ, V. Wright, I. Georgakoudi, and T. Schnelldorfer, "Two-photon images reveal unique texture features for label-free identification of ovarian cancer peritoneal metastases," Biomed Opt Express **10**(9), 4479 (2019).
13. K. Chansky, J. P. Sculier, J. J. Crowley, D. Giroux, J. Van Meerbeeck, and P. Goldstraw, "The International Association for the Study of Lung Cancer Staging Project: Prognostic Factors and Pathologic TNM Stage in Surgically Managed Non-small Cell Lung Cancer," Journal of Thoracic Oncology **4**(7), 792–801 (2009).
14. P. Goldstraw, K. Chansky, J. Crowley, R. Rami-Porta, H. Asamura, W. E. E. Eberhardt, A. G. Nicholson, P. Groome, A. Mitchell, V. Bolejack, D. Ball, D. G. Beer, R. Beyruti, F. Detterbeck, J. Edwards, F. Galateau-Sallé, D. Giroux, F. Gleeson, J. Huang, C. Kennedy, J. Kim, Y. T. Kim, L. Kingsbury, H. Kondo, M. Krasnik, K. Kubota, A. Lerut, G. Lyons, M. Marino, E. M. Marom, J. Van Meerbeeck, T. Nakano, A. Nowak, M. Peake, T. Rice, K. Rosenzweig, E. Ruffini, V. Rusch, N. Saijo, P. Van Schil, J. P. Sculier, L. Shemanski, K. Stratton, K.

Suzuki, Y. Tachimori, C. F. Thomas, W. Travis, M. S. Tsao, A. Turrisi, J. Vansteenkiste, H. Watanabe, Y. L. Wu, P. Baas, J. Erasmus, S. Hasegawa, K. Inai, K. Kernstine, H. Kindler, L. Krug, K. Nackaerts, H. Pass, D. Rice, C. Falkson, P. L. Filosso, G. Giaccone, K. Kondo, M. Lucchi, M. Okumura, E. Blackstone, F. Abad Cavaco, E. Ansótegui Barrera, J. Abal Arca, I. Parente Lamelas, A. Arnau Obrer, R. Guijarro Jorge, G. K. Bascom, A. I. Blanco Orozco, M. González Castro, M. G. Blum, D. Chimondeguy, V. Cvijanovic, S. Defranchi, B. De Olaiz Navarro, I. Escobar Campuzano, I. Macía Vidueira, E. Fernández Araujo, F. Andreo García, K. M. Fong, G. Francisco Corral, S. Cerezo González, J. Freixinet Gilart, L. García Arangüena, S. García Barajas, P. Girard, T. Goksel, M. T. González Budiño, G. González Casaurrán, J. A. Gullón Blanco, J. Hernández Hernández, H. Hernández Rodríguez, J. Herrero Collantes, M. Iglesias Heras, J. M. Izquierdo Elena, E. Jakobsen, S. Kostas, P. León Atance, A. Núñez Ares, M. Liao, M. Losanovscky, R. Magaroles, L. De Esteban Júlvez, M. Mariñán Gorospe, B. McCaughan, R. Melchor Íñiguez, L. Miravet Sorribes, S. Naranjo Gozalo, C. Álvarez De Arriba, M. Núñez Delgado, J. Padilla Alarcón, J. C. Peñalver Cuesta, J. S. Park, M. J. Pavón Fernández, M. Rosenberg, J. S. Sánchez De Cos Escuín, A. Saura Vinuesa, T. E. Strand, M. Serra Mitjans, D. Subotic, S. Swisher, R. Terra, C. Thomas, K. Tournoy, M. Velasquez, Y. L. Wu, and K. Yokoi, "The IASLC Lung Cancer Staging Project: Proposals for Revision of the TNM Stage Groupings in the Forthcoming (Eighth) Edition of the TNM Classification for Lung Cancer," Journal of Thoracic Oncology **11**(1), 39–51 (2016).

15. R. Rami-Porta, V. Bolejack, J. Crowley, D. Ball, J. Kim, G. Lyons, T. Rice, K. Suzuki, C. F. Thomas, W. D. Travis, and Y. L. Wu, "The IASLC Lung Cancer Staging Project: Proposals for the Revisions of the T Descriptors in the Forthcoming Eighth Edition of the TNM Classification for Lung Cancer," Journal of Thoracic Oncology **10**(7), 990–1003 (2015).
16. J. Deng, M. Zhao, T. Wang, Y. She, J. Wu, H. E, J. Gao, X. Sun, G. Jiang, Y. Zhu, D. Xie, and C. Chen, "A modified T categorization for part-solid lesions in Chinese patients with clinical stage I Non–small cell lung cancer," Lung Cancer **145**, 33–39 (2020).
17. P. Wang, Z. Luo, C. Luo, and T. Wang, "Application of a Comprehensive Model Based on CT Radiomics and Clinical Features for Postoperative Recurrence Risk Prediction in Non-small Cell Lung Cancer," Acad Radiol (2024).
18. X. Wang, A. Janowczyk, Y. Zhou, R. Thawani, P. Fu, K. Schalper, V. Velcheti, and A. Madabhushi, "Prediction of recurrence in early stage non-small cell lung cancer using computer extracted nuclear features from digital H&E images," Scientific Reports 2017 7:1 **7**(1), 1–10 (2017).
19. J. Ran, R. Cao, J. Cai, T. Yu, D. Zhao, and Z. Wang, "Development and Validation of a Nomogram for Preoperative Prediction of Lymph Node Metastasis in Lung Adenocarcinoma Based on Radiomics Signature and Deep Learning Signature," Front Oncol **11**, 585942 (2021).
20. T. Lin, J. Mai, M. Yan, Z. Li, X. Quan, and X. Chen, "A nomogram based on ct deep learning signature: A potential tool for the prediction of overall survival in resected non-small cell lung cancer patients," Cancer Manag Res **13**, 2897–2906 (2021).
21. T. P. Coroller, V. Agrawal, E. Huynh, V. Narayan, S. W. Lee, R. H. Mak, and H. J. W. L. Aerts, "Radiomic-Based Pathological Response Prediction from Primary Tumors and Lymph Nodes in NSCLC," Journal of Thoracic Oncology **12**(3), 467–476 (2017).
22. C. T. Hensley, B. Faubert, Q. Yuan, N. Lev-Cohain, E. Jin, J. Kim, L. Jiang, B. Ko,

R. Skelton, L. Loudat, M. Wodzak, C. Klimko, E. McMillan, Y. Butt, M. Ni, D. Oliver, J. Torrealba, C. R. Malloy, K. Kernstine, R. E. Lenkinski, and R. J. DeBerardinis, "Metabolic Heterogeneity in Human Lung Tumors," Cell (2016).

23. A. J. Walsh, R. S. Cook, H. C. Manning, D. J. Hicks, A. Lafontant, C. L. Arteaga, and M. C. Skala, "Optical Metabolic Imaging Identifies Glycolytic Levels, Subtypes, and Early-Treatment Response in Breast Cancer," Cancer Res **73**(20), 6164–6174 (2013).
24. K. P. Quinn, E. Bellas, N. Fourligas, K. Lee, D. L. Kaplan, and I. Georgakoudi, "Characterization of metabolic changes associated with the functional development of 3D engineered tissues by non-invasive, dynamic measurement of individual cell redox ratios," Biomaterials (2012).
25. W. Denk, J. H. Strickler, and W. W. Webb, "Two-photon laser scanning fluorescence microscopy," Science (1979) (1990).
26. W. R. Zipfel, R. M. Williams, R. Christiet, A. Y. Nikitin, B. T. Hyman, and W. W. Webb, "Live tissue intrinsic emission microscopy using multiphoton-excited native fluorescence and second harmonic generation," Proc Natl Acad Sci U S A (2003).
27. K. P. Quinn, G. V. Sridharan, R. S. Hayden, D. L. Kaplan, K. Lee, and I. Georgakoudi, "Quantitative metabolic imaging using endogenous fluorescence to detect stem cell differentiation," Sci Rep (2013).
28. N. Ramanujam, R. Richards-Kortum, S. Thomsen, A. Mahadevan-Jansen, M. Follen, and B. Chance, "Low Temperature Fluorescence Imaging of Freeze-trapped Human Cervical Tissues," Opt Express (2001).
29. R. Drezek, C. Brookner, I. Pavlova, I. Boiko, A. Malpica, R. Lotan, M. Follen, and R. Richards-Kortum, "Autofluorescence Microscopy of Fresh Cervical-Tissue Sections Reveals Alterations in Tissue Biochemistry with Dysplasia¶," Photochem Photobiol (2001).
30. M. C. Skala, K. M. Riching, A. Gendron-Fitzpatrick, J. Eickhoff, K. W. Eliceiri, J. G. White, and N. Ramanujam, "In vivo multiphoton microscopy of NADH and FAD redox states, fluorescence lifetimes, and cellular morphology in precancerous epithelia," Proc Natl Acad Sci U S A (2007).
31. A. Varone, J. Xylas, K. P. Quinn, D. Pouli, G. Sridharan, M. E. McLaughlin-Drubin, C. Alonzo, K. Lee, K. Münger, and I. Georgakoudi, "Endogenous two-photon fluorescence imaging elucidates metabolic changes related to enhanced glycolysis and glutamine consumption in precancerous epithelial tissues," Cancer Res (2014).
32. A. J. Walsh, R. S. Cook, M. E. Sanders, L. Aurisicchio, G. Ciliberto, C. L. Arteaga, and M. C. Skala, "Quantitative optical imaging of primary tumor organoid metabolism predicts drug response in breast cancer," Cancer Res **74**(18), 5184 (2014).
33. P. F. Favreau, J. He, D. A. Gil, D. A. Deming, J. Huisken, and M. C. Skala, "Label-free redox imaging of patient-derived organoids using selective plane illumination microscopy," Biomed Opt Express **11**(5), 2591 (2020).
34. J. T. Sharick, C. M. Walsh, C. M. Sprackling, C. A. Pasch, D. L. Pham, K. Esbona, A. Choudhary, R. Garcia-Valera, M. E. Burkard, S. M. McGregor, K. A. Matkowskyj, A. A. Parikh, I. M. Meszoely, M. C. Kelley, S. Tsai, D. A. Deming, and M. C. Skala, "Metabolic Heterogeneity in Patient Tumor-Derived Organoids by Primary Site and Drug Treatment," Front Oncol **10**, 529045 (2020).
35. L. Z. Li, R. Zhou, H. N. Xu, L. Moon, T. Zhong, E. J. Kim, H. Qiao, R. Reddy, D. Leeper, B. Chance, and J. D. Glickson, "Quantitative Magnetic Resonance And Optical Imaging Biomarkers Of Melanoma Metastatic Potential," Proc Natl Acad Sci U S A (2009).

36. H. N. Xu, S. Nioka, J. D. Glickson, B. Chance, and L. Z. Li, "Quantitative mitochondrial redox imaging of breast cancer metastatic potential," J Biomed Opt (2010).
37. K. Alhallak, S. V. Jenkins, D. E. Lee, N. P. Greene, K. P. Quinn, R. J. Griffin, R. P. M. Dings, and N. Rajaram, "Optical imaging of radiation-induced metabolic changes in radiation-sensitive and resistant cancer cells," J Biomed Opt (2017).
38. J. R. Lakowicz, H. Szmacinski, K. Nowaczyk, and M. L. Johnson, "Fluorescence lifetime imaging of free and protein-bound NADH," Proc Natl Acad Sci U S A (1992).
39. L. C. Chen, W. R. Lloyd, C. W. Chang, D. Sud, and M. A. Mycek, "Fluorescence lifetime imaging microscopy for quantitative biological imaging," in *Methods in Cell Biology* (2013).
40. O. I. Kolenc and K. P. Quinn, "Evaluating cell metabolism through autofluorescence imaging of NAD(P)H and FAD," Antioxid Redox Signal (2019).
41. M. C. Skala, K. M. Riching, D. K. Bird, A. Gendron-Fitzpatrick, J. Eickhoff, K. W. Eliceiri, P. J. Keely, and N. Ramanujam, "In vivo multiphoton fluorescence lifetime imaging of protein-bound and free nicotinamide adenine dinucleotide in normal and precancerous epithelia," J Biomed Opt (2007).
42. M. Wang, F. Tang, X. Pan, L. Yao, X. Wang, Y. Jing, J. Ma, G. Wang, and L. Mi, "Rapid diagnosis and intraoperative margin assessment of human lung cancer with fluorescence lifetime imaging microscopy," BBA Clin (2017).
43. I. Pavlova, K. R. Hume, S. A. Yazinski, J. Flanders, T. L. Southard, R. S. Weiss, and W. W. Webb, "Multiphoton microscopy and microspectroscopy for diagnostics of inflammatory and neoplastic lung," J Biomed Opt (2012).
44. K. P. Quinn, E. C. Leal, A. Tellechea, A. Kafanas, M. E. Auster, A. Veves, and I. Georgakoudi, "Diabetic wounds exhibit distinct microstructural and metabolic heterogeneity through label-free multiphoton microscopy," J Invest Dermatol **136**(1), 342 (2016).
45. G. A. Snyder, S. Kumar, G. K. Lewis, and K. Ray, "Two-photon fluorescence lifetime imaging microscopy of NADH metabolism in HIV-1 infected cells and tissues," Front Immunol **14**, 1213180 (2023).
46. J. D. Jones, H. E. Ramser, A. E. Woessner, and K. P. Quinn, "In vivo multiphoton microscopy detects longitudinal metabolic changes associated with delayed skin wound healing," Commun Biol (2018).
47. A. J. Walsh, K. M. Poole, C. L. Duvall, and M. C. Skala, "Ex vivo optical metabolic measurements from cultured tissue reflect in vivo tissue status," J Biomed Opt **17**(11), 116015 (2012).
48. B. D. Shields, F. Mahmoud, E. M. Taylor, S. D. Byrum, D. Sengupta, B. Koss, G. Baldini, S. Ransom, K. Cline, S. G. Mackintosh, R. D. Edmondson, S. Shalin, and A. J. Tackett, "Indicators of responsiveness to immune checkpoint inhibitors," Sci Rep **7**, (2017).
49. B. D. Shields, B. Koss, E. M. Taylor, A. J. Storey, K. L. West, S. D. Byrum, S. G. Mackintosh, R. Edmondson, F. Mahmoud, S. C. Shalin, and A. J. Tackett, "Loss of E-cadherin inhibits CD103 antitumor activity and reduces checkpoint blockade responsiveness in melanoma," Cancer Res **79**(6), 1113–1123 (2019).
50. A. I. Nesvizhskii, A. Keller, E. Kolker, and R. Aebersold, "A statistical model for identifying proteins by tandem mass spectrometry," Anal Chem **75**(17), 4646–4658 (2003).
51. "Investigating the relationship between hypoxia, hypoxia-inducible factor 1, and the optical redox ratio in response to radiation therapy," https://www.spiedigitallibrary.org/journals/biophotonics-discovery/volume-1/issue-

01/015003/Investigating-the-relationship-between-hypoxia-hypoxia-inducible-factor-1-and/10.1117/1.BIOS.1.1.015003.full#_=_.
52. A. L. Visbal, B. A. Williams, F. C. Nichols, R. S. Marks, J. R. Jett, M. C. Aubry, E. S. Edell, J. A. Wampfler, J. R. Molina, and P. Yang, "Gender differences in non–small-cell lung cancer survival: an analysis of 4,618 patients diagnosed between 1997 and 2002," Ann Thorac Surg **78**(1), 209–215 (2004).
53. F. L. Kinoshita, Y. Ito, T. Morishima, I. Miyashiro, and T. Nakayama, "Sex differences in lung cancer survival: long-term trends using population-based cancer registry data in Osaka, Japan," Jpn J Clin Oncol **47**(9), 863–869 (2017).
54. F. Tas, R. Ciftci, L. Kilic, and S. Karabulut, "Age is a prognostic factor affecting survival in lung cancer patients," Oncol Lett **6**(5), 1507 (2013).
55. F. R. Hirsch, A. Spreafico, S. Novello, M. D. Wood, L. Simms, and M. Papotti, "The Prognostic and Predictive Role of Histology in Advanced Non-small Cell Lung Cancer: A Literature Review," Journal of Thoracic Oncology **3**(12), 1468–1481 (2008).
56. B. Hao, T. Fan, J. Xiong, L. Zhang, Z. Lu, B. Liu, H. Meng, R. He, N. Li, and Q. Geng, "The Prognostic Significance of the Histological Types in Patients With Nonsmall Cell Lung Cancer ≤2 cm," Front Surg **8**, 721567 (2021).
57.C. Szegedy, S. Ioffe, V. Vanhoucke, and A. Alemi, “Inception-v4, Inception-ResNet and the Impact of Residual Connections on Learning,” CoRR, vol. abs/1602.07261 (2016).
58.S. Schiele, T.T. Arndt, B. Martin, S. Miller, S. Bauer, B.M. Banner, E.M. Brendel, G. Schenkirsch, M. Anthuber, R. Huss, B. Märkl, and G. Müller, “Deep Learning Prediction of Metastasis in Locally Advanced Colon Cancer Using Binary Histologic Tumor Images,” Cancers (Basel), 13(9):2074 (2021).

57. K. Alhallak, L. G. Rebello, T. J. Muldoon, K. P. Quinn, and N. Rajaram, "Optical redox ratio identifies metastatic potential-dependent changes in breast cancer cell metabolism," Biomed Opt Express (2016).
58. J. A. Hellyer, S. K. Padda, M. Diehn, and H. A. Wakelee, "Clinical Implications of KEAP1-NFE2L2 Mutations in NSCLC," Journal of Thoracic Oncology **16**(3), 395–403 (2021).
59. T. Takahashi, M. Sonobe, T. Menju, E. I. Nakayama, N. Mino, S. Iwakiri, S. Nagai, K. Sato, R. Y. O. Miyahara, K. Okubo, T. Hirata, H. Date, and H. Wada, "Mutations in Keap1 are a potential prognostic factor in resected non-small cell lung cancer," J Surg Oncol **101**(6), 500–506 (2010).
60. J. T. Sharick, C. M. Walsh, C. M. Sprackling, C. A. Pasch, D. L. Pham, K. Esbona, A. Choudhary, R. Garcia-Valera, M. E. Burkard, S. M. McGregor, K. A. Matkowskyj, A. A. Parikh, I. M. Meszoely, M. C. Kelley, S. Tsai, D. A. Deming, and M. C. Skala, "Metabolic Heterogeneity in Patient Tumor-Derived Organoids by Primary Site and Drug Treatment," Front Oncol (2020).
61. A. T. Shah, T. M. Heaster, and M. C. Skala, "Metabolic imaging of head and neck cancer organoids," PLoS One (2017).
62. A. J. Walsh, R. S. Cook, M. E. Sanders, L. Aurisicchio, G. Ciliberto, C. L. Arteaga, and M. C. Skala, "Quantitative optical imaging of primary tumor organoid metabolism predicts drug response in breast cancer," Cancer Res (2014).
63. A. Peng, H. N. Xu, L. Moon, P. Zhang, and L. Z. Li, "Quantitative Optical Redox Imaging of Melanoma Xenografts with Different Metastatic Potentials," Cancers 2024, Vol. 16, Page 1669 **16**(9), 1669 (2024).
64. C.-C. Wang, F.-C. Li, R.-J. Wu, V. A. Hovhannisyan, W.-C. Lin, S.-J. Lin, P. T. C. So, and C.-Y. Dong, "Differentiation of normal and cancerous lung tissues by

multiphoton imaging," J Biomed Opt (2009).
65. I. Pavlova, K. R. Hume, S. A. Yazinski, R. M. Peters, R. S. Weiss, and W. W. Webb, "Multiphoton microscopy as a diagnostic imaging modality for lung cancer," in *Multiphoton Microscopy in the Biomedical Sciences X* (2010).
66. M. Jain, N. Narula, A. Aggarwal, B. Stiles, M. M. Shevchuk, J. Sterling, B. Salamoon, V. Chandel, W. W. Webb, N. K. Altorki, and S. Mukherjee, "Multiphoton microscopy: A potential “optical biopsy” tool for real-time evaluation of lung tumors without the need for exogenous contrast agents," Arch Pathol Lab Med (2014).
67. L. M. G. Huizen, T. Radonic, F. Mourik, D. Seinstra, C. Dickhoff, J. M. A. Daniels, I. Bahce, J. T. Annema, and M. L. Groot, "Compact portable multiphoton microscopy reveals histopathological hallmarks of unprocessed lung tumor tissue in real time," Transl Biophotonics (2020).
68. L. M. Solis, C. Behrens, W. Dong, M. Suraokar, N. C. Ozburn, C. A. Moran, A. H. Corvalan, S. Biswal, S. G. Swisher, B. N. Bekele, J. D. Minna, D. J. Stewart, and I. I. Wistuba, "Nrf2 and Keap1 abnormalities in non-small cell lung carcinoma and association with clinicopathologic features," Clinical Cancer Research **16**(14), 3743–3753 (2010).
69. M. Gong, Y. Li, X. Ye, L. Zhang, Z. Wang, X. Xu, Y. Shen, and C. Zheng, "Loss-of-function mutations in KEAP1 drive lung cancer progression via KEAP1/NRF2 pathway activation," Cell Commun Signal **18**(1), (2020).
70. A. S. Agyeman, R. Chaerkady, P. G. Shaw, N. E. Davidson, K. Visvanathan, A. Pandey, and T. W. Kensler, "Transcriptomic and proteomic profiling of KEAP1 disrupted and sulforaphane-treated human breast epithelial cells reveals common expression profiles," Breast Cancer Res Treat **132**(1), 175–187 (2012).
71. M. Y. Song, D. Y. Lee, K. S. Chun, and E. H. Kim, "The Role of NRF2/KEAP1 Signaling Pathway in Cancer Metabolism," Int J Mol Sci **22**(9), (2021).
72. E. Panieri, P. Telkoparan-Akillilar, S. Suzen, and L. Saso, "The NRF2/KEAP1 Axis in the Regulation of Tumor Metabolism: Mechanisms and Therapeutic Perspectives," Biomolecules **10**(5), (2020).
73. P. Koppula, K. Olszewski, Y. Zhang, L. Kondiparthi, X. Liu, G. Lei, M. Das, B. Fang, M. V. Poyurovsky, and B. Gan, "KEAP1 deficiency drives glucose dependency and sensitizes lung cancer cells and tumors to GLUT inhibition," iScience **24**(6), 102649 (2021).
74. T. Weiss-Sadan, M. Ge, M. Hayashi, M. Gohar, C. H. Yao, A. de Groot, S. Harry, A. Carlin, H. Fischer, L. Shi, T. Y. Wei, C. H. Adelmann, K. Wolf, T. Vornbäumen, B. R. Dürr, M. Takahashi, M. Richter, J. Zhang, T. Y. Yang, V. Vijay, D. E. Fisher, A. N. Hata, M. C. Haigis, R. Mostoslavsky, N. Bardeesy, T. Papagiannakopoulos, and L. Bar-Peled, "NRF2 activation induces NADH-reductive stress, providing a metabolic vulnerability in lung cancer," Cell Metab **35**(3), 487-503.e7 (2023).
75. D. E. Lee, K. Alhallak, S. V. Jenkins, I. Vargas, N. P. Greene, K. P. Quinn, R. J. Griffin, R. P. M. Dings, and N. Rajaram, "A Radiosensitizing Inhibitor of HIF-1 alters the Optical Redox State of Human Lung Cancer Cells In Vitro," Sci Rep **8**(1), (2018).
76. A. Podsednik, A. Jacob, L. Z. Li, and H. N. Xu, "Relationship between Optical Redox Status and Reactive Oxygen Species in Cancer Cells," React Oxyg Species (Apex) **9**(26), 95 (2020).